

Multi-Tb/s-per-Fiber Coherent Co-Packaged Optical Interfaces for Data Center Switches

Brandon Buscaino , *Student Member, IEEE*, Brian D. Taylor, and Joseph M. Kahn, *Fellow, IEEE*

Abstract—Co-packaging of optical and electronic interfaces inside data center switches has been proposed to reduce the system-level power consumption and support higher density, higher capacity optical links. However, co-locating electronics and optics increases optical losses and exposes lasers, (de)multiplexers and other components to temperature fluctuations. We propose a design for co-packaged interfaces using coherent detection and wide-passband (de)multiplexers to increase the total bit rate per fiber in the presence of demultiplexer center frequency shifts up to ± 150 GHz. We compare direct and coherent detection systems within this architecture and demonstrate that unamplified coherent links can provide over 20 dB higher loss budget than direct detection links at 400 Gb/s per fiber. Moreover, coherent links can offer far higher bit rates per fiber. For example, in the presence of (de)multiplexer center frequency shifts of up to ± 150 GHz, DP-QPSK links can scale to over 5 Tb/s per fiber, while four pulse amplitude modulation (PAM) links are optical bandwidth limited to ~ 400 Gb/s per fiber. We quantify signal path loss and optical signal-to-noise ratio budgets when optical amplifiers, limited to eye-safe output powers, are used to compensate for losses of fibers or optical switches. While the loss and SNR budgets of direct detection links may be improved by optical amplifiers, these systems cannot scale to high bit rates per fiber because large channel spacings are required to accommodate (de)multiplexer center frequency shifts. For example, amplified 4-PAM links can scale to less than 1.3 Tb/s per fiber, while amplified DP-QPSK links can scale to greater than 12.8 Tb/s per fiber.

Index Terms—Coherent detection, co-packaged optics, optical fiber communication, wavelength division multiplexing.

I. INTRODUCTION

INTRA-DATA center Internet Protocol (IP) traffic represents over 90% of global IP traffic and is expected to grow at a compound annual growth rate of 25% until 2021 [1]. The projected increase in intra-data center traffic has forced hyperscale data centers to rapidly increase the switching capacity of electrical switches inside data centers. For example, current state-of-the-art electrical switches can support 12.8 Tb/s switching capacity,

but over the next 5–10 years, these switches are expected to support 51.2 Tb/s or higher [2].

Traditionally, increases in data center switching capacity have been supported by increasing the symbol rate or number of parallel fiber pairs. However, these solutions are now posing significant technical challenges. Scaling the symbol rate is the least viable solution because of limited component electrical bandwidth [3]. Even when electrical components achieving higher bandwidths can be fabricated, they often consume an excessive amount of electrical power for use inside data centers [4]. Scaling the number of fiber pairs inside data centers is likewise difficult. Current intra-data center links operate at 100 Gb/s or 200 Gb/s per fiber. While 400 Gb/s-per-fiber standards have been approved by the IEEE 802.3bs task force, commercial 400 Gb/s-per-fiber options are limited [5], [6]. At these per-fiber bit rates, rack-mounted switches will require hundreds of fiber connections. Data centers that rely on pluggable transceivers may soon find it difficult to fit the required number of transceivers into a single rack [7].

Another alternative to increasing the switch interface capacity is to increase the modulation order. Direct detection-compatible formats, such as non-return-to-zero on-off keying (NRZ-OOK) or M-ary pulse amplitude modulation (M-PAM) are common inside data centers due to their low component count, simplicity, and low power consumption. For example, 4-PAM was recently adopted by the IEEE 802.3bs task force. However, direct detection-compatible formats offer poor receiver sensitivity as they are scaled to 4-PAM and higher orders. Coherent detection and compatible formats, such as quaternary phase shift keying (QPSK) or M-ary quadrature amplitude modulation (M-QAM), provide superior receiver sensitivity, which may prove important for future links that have high optical losses.

The last commonly considered option for increasing the capacity of intra-data center links is increasing the number of optical wavelengths per fiber. Ethernet standards that leverage additional wavelengths, such as 400G-GBASE-LR8, have been successful at introducing up to eight wavelengths per fiber, but have not scaled to higher wavelength counts due to the poor receiver sensitivity of direct detection [8]. Additionally, eye-safety constraints inside data centers limit the optical power per fiber, exacerbating the issue of poor receiver sensitivity.

Co-packaging of the optics and electronics inside data center switches has been proposed to address the issues of total component footprint and electrical power consumption currently faced by pluggable transceiver architectures. Co-packaged solutions,

Manuscript received January 15, 2019; revised April 2, 2019; accepted May 7, 2019. Date of publication May 15, 2019; date of current version June 10, 2019. This work was supported by Facebook, Inc., Maxim Integrated, and National Science Foundation under Grant ECCS-1740291 E2CDA. (Corresponding author: Brandon Buscaino.)

B. Buscaino and J. M. Kahn are with the Department of Electrical Engineering, Stanford University, Stanford, CA 94305 USA (e-mail: buscaino@stanford.edu; jmk@ee.stanford.edu).

B. D. Taylor is with Inphi Corporation, Santa Clara, CA 95054 USA (e-mail: btaylor@inphi.com).

Color versions of one or more of the figures in this paper are available online at <http://ieeexplore.ieee.org>.

Digital Object Identifier 10.1109/JLT.2019.2916988

which may be composed of one or more photonic integrated circuits (PICs), are naturally suited for wavelength-division-multiplexed (WDM) systems due to the maturing fabrication technologies surrounding silicon photonics [7]. Moreover, by eliminating many lossy electrical switch interfaces, co-packaged optics can reduce system-level electrical power consumption by up to 30% [5].

However, integrating optics and electronics onto a single PIC can introduce significant technical challenges. Due to the bursty nature of intra-data center traffic and high power consumption of the switching circuits, the thermal environment of the co-packaged switch can fluctuate rapidly. For example, 12.8 Tb/s switches can experience temperature fluctuations of greater than 1 °C per second, with peak-to-peak temperature excursions of over 15 °C. Sensitive optical components such as lasers and (de)multiplexers, if integrated near the electronics, may perform poorly in the unpredictable thermal environment, causing degraded performance or link failure.

Additionally, integrated optical devices often have high optical insertion losses. Fiber-to-PIC coupling, waveguide bends, modulators, (de)multiplexers and other components can lead to losses of tens of dB between a transmit laser and receive photodetector. Future data center architectures may employ optical switching [9], adding to the optical losses.

In this paper we present a scalable system-level architecture for data center switching that relies on coherent detection, wide-passband (de)multiplexers, and an external multi-wavelength source (MWS) in order to increase the capacity per fiber, while satisfying eye-safety constraints. The proposed architecture is compatible with co-packaged optical interfaces that may have large temperature fluctuations and high optical insertion losses. We analyze links based on direct detection and coherent detection to determine the optical loss budgets for various per-fiber bit rates and amplification schemes.

The remainder of the paper is organized as follows. In Section II, we discuss and quantify the challenges of highly integrated optical interfaces, such as temperature fluctuations and optical losses. In Section III we describe the proposed data center architecture on both the PIC level and system level. In Section IV, we perform noise analyses for direct and coherent detection systems under the proposed architecture. In Section V, we present numerical results for optical loss budgets and optical signal-to-noise ratio (OSNR) budgets. We present conclusions in Section VI.

II. CHALLENGES OF HIGHLY INTEGRATED OPTICAL INTERFACES

The various optical integration platforms under development offer different advantages and drawbacks for co-packaged interfaces. Silica-on-silicon (SoS) technology, which uses silica waveguides, is tolerant to temperature fluctuations due to the low thermo-optic coefficient of silica. Owing to the low index contrast between the silica waveguides and the silicon substrate, however, light is poorly confined in the waveguides, resulting in devices that have a large footprint and high power consumption [10].

Waveguides made in silicon nitride, on the other hand, exhibit lower loss and have a higher index contrast than silica waveguides, at the expense of an increased thermo-optic coefficient [11]. Silicon waveguides, fabricated with silicon-on-insulator (SOI) technology, have a higher thermo-optic coefficient than silicon nitride waveguides, but have larger index contrast and are compatible with complementary metal-oxide-semiconductor (CMOS) fabrication techniques. In this paper, we focus on the SOI material platform, as it is the most likely platform to be commercialized in the coming decade. Unfortunately, it has the highest temperature sensitivity. The results presented are valid for other material platforms with less temperature sensitivity, as will be shown in Section V.

A. Temperature Fluctuations

1) *Optical Sources*: The light source is one of the most temperature-sensitive components in an optical link. Temperature fluctuations induce a drift in the output frequency of integrated lasers by more than 100 GHz/°C [12]. While temperature-dependent shifts of this order may be tolerable for systems using four or eight wavelengths, links that operate with tens of distinct wavelengths will likely require stabilized carriers. Although it is possible to stabilize lasers with complex athermal designs [13] or by using thermo-electric cooling, the increase in system complexity, footprint, and power consumption of these systems is likely to be prohibitive.

Alternatively, a multi-wavelength carrier (MWC) can be input-coupled onto the PIC from an external MWS via facet or grating couplers. The MWS may be a high-power optical frequency comb or a bank of frequency-stabilized lasers coupled to a multiplexer. In either case, the output MWC is an optical field composed of equally spaced carriers of nominally equal power. Using an external MWS provides stable, high-power optical carriers without the challenges of integration on a PIC with high temperature fluctuations. In this paper, we will assume that the MWC emits in the C band so that low-cost erbium-doped fiber amplifiers (EDFAs) can be used in system architectures requiring amplification.

2) *(De)multiplexers*: Wavelength multiplexers and demultiplexers are critical components for WDM optical links. There are many methods of (de)multiplexing optical signals, ranging from nested Mach-Zehnder interferometers and cascaded ring resonators to arrayed waveguide gratings (AWGs) [14]. In this paper, we consider only AWGs, owing to their low loss, small footprint, and ability to (de)multiplex many wavelengths [15].

An AWG couples an input optical field into arrayed waveguides of different path lengths, inducing interference at the output. When the temperature of an AWG changes, the relative path lengths of the arrayed waveguides changes, causing a shift in the (de)multiplexer center frequency. Typical values of the center frequency shift are 1 GHz/°C for silica AWGs and 10 GHz/°C for SOI AWGs [11]. While the exact temperature profiles of future switches are implementation-dependent, temperature swings of $\pm 15^\circ\text{C}$ may be unavoidable. For this reason, we will consider (de)multiplexer center frequency shifts up to ± 150 GHz.

TABLE I
INSERTION LOSSES OF INTEGRATED COMPONENTS

Component	Insertion Loss	Reference
Input/Output Coupler	-1.5 dB	[17] [18]
Power Splitter and Combiner	-1 dB	[19] [20]
Waveguide (several cm)	-2 dB	[21] [22]
AWG (De)Multiplexer	-3 dB	[23] [24]
Modulator	-5 dB	[25] [26]

If the available optical bandwidth for the link is large, temperature effects can be avoided by placing optical carriers hundreds of GHz apart. In many system designs, however, the usable bandwidth is limited, as in systems using C-band EDFAs, so it is desirable to space the optical carriers more closely.

Unlike the MWS, which may be placed away from the PIC, AWGs are unlikely to be removed from the PIC because the size of the co-packaged switch may increase significantly due to the number of necessary fiber-to-PIC couplers. While numerous athermal AWG designs exist, they often increase the AWG footprint or introduce additional materials to the fabrication process, increasing cost [16].

B. Insertion Losses

When compared to their bulk equivalent, integrated devices often exhibit high insertion losses due to waveguide roughness and bending, doping added to enable quasi-electro-optic modulation, modal field mismatch, etc. [27]. Moreover, PIC loss can depend on per-fiber capacity and the optical bandwidth of integrated components. For example, systems with lower per-fiber bit rates can utilize fiber-to-PIC couplers with narrower optical bandwidth, achieving lower loss. Alternatively, systems with higher per-fiber bit rates may use wavelengths outside the optical bandwidth of fiber-to-PIC couplers or AWGs. Additionally, systems that require polarization control, such as those using coherent detection, will require polarization-diverse couplers and polarization beam splitters that may increase the loss.

In this paper, we analyze data center switch capacities that lie generations in the future. Thus, we will focus on state-of-the-art devices and their losses in the rest of this paper. Table I shows approximate insertion loss values of the necessary on-PIC devices with references to recent work exhibiting the device performance. The loss values in Table I are generally larger than the minimum values reported to account for nonuniform loss profiles over the wide optical bandwidth studied in this paper. To provide a fair comparison between high- and low-capacity systems using direct and coherent detection, we assume a fixed transmitter and receiver PIC loss across all systems. We discuss in later sections how the results may be interpreted for systems that have different on-PIC losses than those assumed in this paper.

III. LINK ARCHITECTURE

A. Coherent Co-Packaged PIC

1) *Architecture*: Figure 1 presents a generalized design of a co-packaged data center switch. An electrical switching

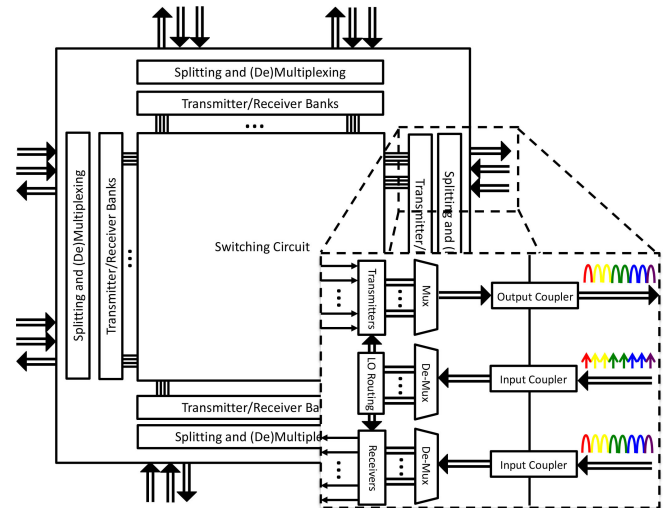


Fig. 1. Schematic of a co-packaged data center switch. The on-PIC optical components in the transmitter and receiver banks are co-packaged with the switching circuit to minimize electrical interface length. An external multi-wavelength source, not shown, serves as the optical source for the output signal and local oscillator for coherent detection. Acronyms: multiplexer (Mux), local oscillator (LO).

circuit at the center of the PIC transmits and receives electrical signals, typically parallel signals at baud rates lower than the optical symbol rate, to banks of optical transmitters and receivers. These devices are kept close to the switching circuit to minimize electrical losses between the switching circuit and PIC.

The inset in Figure 1 shows a magnified view of the PIC. Electrical signals from the switching circuit are modulated onto optical signals, multiplexed, and output-coupled to a single fiber. Similarly, an input WDM signal is demultiplexed and sent to optical receivers where the single-wavelength signals are detected and routed to the switching circuit. The details of the multiplexer and demultiplexer systems will be discussed in detail in Section III-B. Note that a MWC is coupled onto the PIC to serve as both the optical carriers for the WDM signal and as a local oscillator (LO) if coherent detection is used. Future designs may use a single MWS per switch or may use redundant MWSs in order to increase fault tolerance.

From Figure 1 it is clear that input coupling a MWC rather than a multiplicity of single-wavelength carriers is advantageous, because the former obviates the need for waveguide crossings. Alternatively, if single-wavelength sources are coupled onto the PIC and shared across multiple WDM transmitters or receivers, hundreds to thousands of optical waveguide crossings may be necessary, depending on the aggregate switch capacity and bit rate per fiber.

2) *Footprint*: An important consideration for any practical PIC implementation is the device footprint. Significant advances in silicon photonics have been made in recent years enabling low-loss and high-bandwidth grating couplers, power splitters, and (de)multiplexers [18], [19], [24]. These optical devices do not need to be located near the electrical switching circuit because they are connected via low-loss optical waveguides [28]

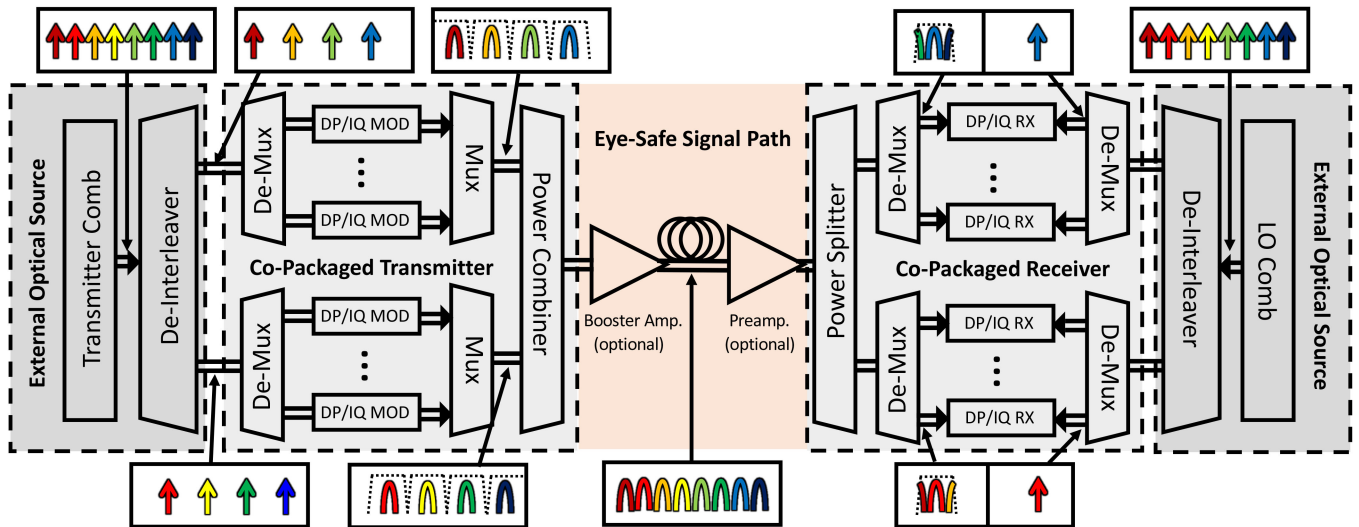


Fig. 2. Temperature-insensitive link architecture, as described in the text. Acronyms: multiplexer (Mux), dual-polarization coherent modulator (DP/IQ MOD), amplifier (AMP), dual-polarization coherent receiver (DP/IQ RX), local oscillator (LO).

and thus can be placed conveniently away from the center of the PIC.

However, opto-electronic devices such as optical modulators and balanced photodetectors must be placed close to the electrical switch in order to minimize the length of electrical interconnects. Lengthy on-PIC electrical interconnects require amplification and can necessitate power-hungry retimers [7]. While coherent optical receivers can be compactly placed near the edge of the electrical switch [29], integrated silicon optical modulators often require phase shifters with lengths ranging from 0.5 to 5 mm, necessitating their careful placement near the switch edge. For example, scaling to a 51.2 Tb/s co-packaged optical interface with an $80 \times 80 \text{ mm}^2$ electrical switching circuit would necessitate an input/output bandwidth density of 160 Gb/s/mm along the switch edge. While optical modulators can be oriented so that the phase shifters are perpendicular to the switch edge, and thus parallel to other phase shifters, electronic crosstalk between modulators can limit the bandwidth density. We show in Section IV-D that architectures utilizing 4-level modulation can achieve an input/output bandwidth density of 175 Gb/s/mm. Links utilizing higher-order modulation formats are desirable because they can increase the bit rate per fiber without drastically increasing the footprint.

3) *Power Consumption*: While systems based on coherent detection have shown remarkable progress in recent years, such as 50+ Gbaud DP-16-QAM systems on silicon platforms [30], [31], power consumption of coherent systems is often higher than those based on direct detection due to power-hungry digital signal processing and additional components such as phase shifters or local oscillators. Yet, recently there have been several demonstrations of coherent transmitters and receivers that operate at low power. For example, DP-QPSK transmitters operating near 30 Gbaud have shown power consumption of under 1 W [32], [33]. Additionally, a fully packaged DP-QPSK transceiver operating at 30 Gbaud has been fabricated that

consumes only 4.5 W [34]. As progress in SOI device technology improves, high-power, high-symbol rate transceivers may be fully realized.

B. Link Design

Figure 2 shows the proposed temperature-independent architecture for coherent links based on co-packaged optical interfaces. The system is designed to use wide-passband AWG (de)multiplexers to tolerate temperature fluctuations, while using coherent detection to minimize crosstalk between neighboring wavelengths. The dashed boxes in Figure 2 show sample spectra at various points in the link, where dotted lines indicate the relevant AWG passband optical transfer functions.

As discussed in Section II-A, the MWS is kept away from the PIC to reduce thermal effects. External to the PIC, the MWS is first de-interleaved to ensure that the on-PIC demultiplexing is able to completely separate the wavelengths. This stage is necessary for coherent systems that utilize the temperature-independent architecture because imperfect demultiplexing of the MWS can result in significant intra-channel crosstalk in the receiver. Although this may increase the total number of fiber-to-PIC couplers, the extra capacity that can be accommodated, as will be shown later, is worth the effort.

After de-interleaving, the MWS is input-coupled to the PIC, where it is demultiplexed, modulated, multiplexed, and output-coupled from the transmitter section of the PIC. Importantly, a power combiner is used after the multiplexers in order to multiplex all desired signals in a manner insensitive to temperature fluctuations. Although this power combiner, and the power splitter in the receiver, introduce additional optical losses into the system, the superior receiver sensitivity of coherent detectors can more than accommodate this additional loss.

After the transmitter PIC, the WDM signal is sent to the eye-safe signal path, which includes at least a section of single-mode

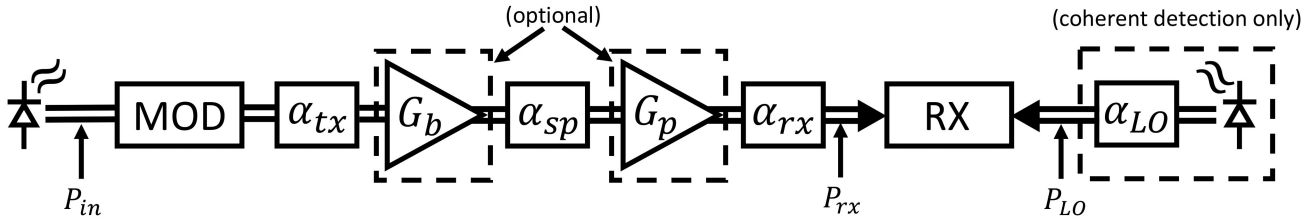


Fig. 3. System model for the proposed intra-data center link architecture. Acronyms: modulator (MOD), transmitter PIC loss (α_{tx}), booster amplifier gain (G_b), signal path optical loss (α_{sp}), preamplifier gain (G_p), receiver PIC loss (α_{rx}), receiver (RX), receiver PIC local oscillator loss (α_{LO}), input laser power (P_{in}), signal power at receiver (P_{rx}), local oscillator power at receiver (P_{LO}).

fiber (SMF). The signal path may also include additional lossy elements, such as optical switches or filters, employed in various advanced data center architectures. In Figure 2, a booster amplifier and preamplifier are shown as optional elements. In later sections we will discuss the implications of including amplifiers in the link.

The WDM signal is then input-coupled to the receiver PIC, where it is demultiplexed with a power splitter and widepassband AWG and routed to an integrated coherent receiver. Another external MWS, located near the receiver PIC, outputs a MWC that is input-coupled, demultiplexed, and used as a single-wavelength LO for the coherent receivers. Here, the received signal may include the desired wavelength as well as other nearby channels. However, coherent detection of the received signal, followed by electrical lowpass filtering, will dramatically reduce the crosstalk, as will be discussed in Section IV-B.

IV. PERFORMANCE ANALYSIS

A. System Model

Figure 3 presents a system model for the proposed link. The transmitter PIC loss, α_{tx} , the signal path loss, α_{sp} , and the receiver PIC loss, α_{rx} , include relevant lumped losses from the device components in Section II-B. An optional booster and preamplifier are included to increase the optical power to the eye-safety limit. In the following section we will analyze coherent and direct detection performance in unamplified and amplified systems. The modulator and receiver blocks are left unspecified, and will be specified for direct detection and coherent detection systems in the following two sections.

B. Coherent Detection

Figure 4 shows the coherent modulator and receiver block diagrams. The coherent modulator (Figure 4 a) is a nested Mach-Zehnder modulator, which is assumed to have negligible IQ imbalance. Figure 4 b shows a block diagram of a coherent receiver, composed of a 90° hybrid, balanced photodetectors, transimpedance amplifiers (TIAs), and lowpass filters (LPFs). The photodetector is a positive-intrinsic-negative (PIN) photodiode as it is the simplest to integrate onto most material platforms and is generally insensitive to temperature fluctuations. After the LPF, the signal is routed to circuits that performs analog-to-digital conversion, digital polarization control, carrier recovery,

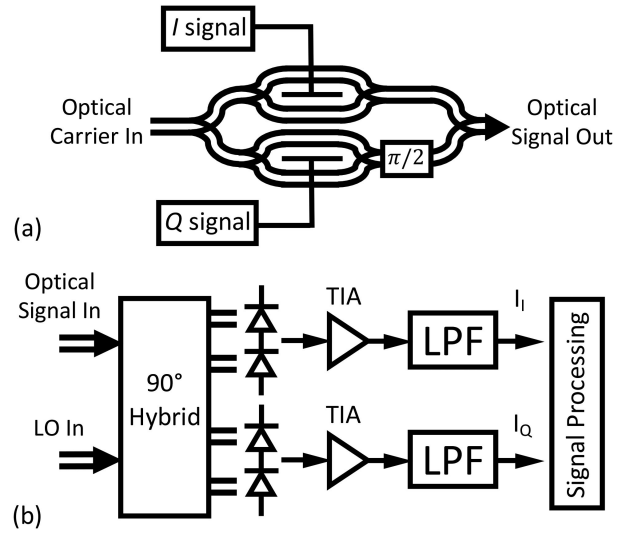


Fig. 4. Coherent modulator and receiver systems. (a) Nested Mach-Zehnder modulator. (b) Coherent receiver comprising a 90° hybrid, balanced photodetectors, transimpedance amplifiers (TIAs), and lowpass filters (LPFs).

and data recovery. We assume that any performance penalty associated with the digital signal processing is negligible.

We analyze the performance of the in-phase (I) component of one polarization component at the receiver, which is representative of all four components, assuming negligible polarization and IQ imbalance. The received root-mean-square (RMS) signal current is

$$I_I = R\sqrt{P_{LO}P_{rx}}/8 \quad (1)$$

where R is the PIN photodetector sensitivity, and P_{rx} and P_{LO} are the average signal power and LO power at the receiver input in two polarizations. Although the detected signal current also contains terms from neighboring channels, these are assumed to be suppressed by lowpass filtering.

The most common noise sources in amplified coherent detection systems are intensity noise, shot noise, amplified spontaneous emission (ASE) noise and thermal noise. Intensity noise is neglected in our analysis; LO intensity noise is suppressed by balanced detection and transmitter intensity noise is suppressed by high link losses. The other noise sources are discussed below.

1) *Shot Noise*: In the proposed architecture, the dominant shot noise arises from the LO. The shot noise can be modeled as Gaussian-distributed with variance given by

$$\begin{aligned}\sigma_{sh}^2 &= q [R(P_{LO} + P_{rx})/2] \Delta f_e \\ &\approx \frac{1}{2} q R P_{LO} \Delta f_e\end{aligned}\quad (2)$$

where q is the electron charge and Δf_e is the effective electrical bandwidth of the receiver.

2) *ASE Noise*: The ASE electric field in each polarization can be modeled as additive white Gaussian noise with one-sided power spectral density (PSD)

$$S_{sp} = n_{sp}(G - 1)h\nu \quad (3)$$

where n_{sp} is the spontaneous emission factor, G is the amplifier gain, and $h\nu$ is the photon energy.

Beating between the LO and the ASE power dominates other ASE beat terms in the receiver. The variance of the noise current due to beating between LO and ASE noise, averaged over the random phase differences between the LO and ASE, is

$$\sigma_{LO,ASE}^2 = \frac{1}{2} R^2 P_{LO} S_{sp} \Delta f_e \quad (4)$$

3) *Thermal Noise*: The variance of the thermal noise current is independent of signal power and given by

$$\sigma_{th}^2 = (4k_B T / R_L) F_n \Delta f_e = i_N^2 \Delta f_e \quad (5)$$

where k_B is the Boltzmann constant, T is the temperature, R_L is the resistive load, and F_n is the electrical noise figure. The noise variance, as shown above, can also be represented by the RMS input-referred noise to the TIA, i_N , as shown above.

4) *BER*: Since all of the noise sources above are approximately Gaussian and signal-independent, estimating the bit-error ratio (BER) from the received signal-to-noise ratio (SNR) will yield accurate results. In this paper we consider square, Gray-coded M-QAM constellations with high SNR. In this case, the BER can be approximated accurately as

$$BER \approx \frac{4(1 - 1/\sqrt{M})}{\log_2(M)} Q\left(\sqrt{\frac{3}{M-1}} \text{SNR}\right) \quad (6)$$

where $\text{SNR} = I_1^2 / (\sigma_{sh}^2 + \sigma_{LO,ASE}^2 + \sigma_{th}^2)$ is the SNR per symbol.

C. Direct Detection Noise Analysis

Figure 5 shows a block diagram of the direct detection modulator and receiver systems. The modulator is a single Mach-Zehnder modulator and the direct detection receiver is a PIN photodiode followed by a TIA and LPF. The average signal current is then $I = R P_{rx}$.

Similar to the case of coherent detection, intensity noise is negligible due to the low optical power at the receiver. Additionally, the shot noise due to the signal is negligible when compared to thermal noise, even in amplified schemes.

Due to square law detection, the statistics of the received signal current in the presence of ASE noise and thermal noise are

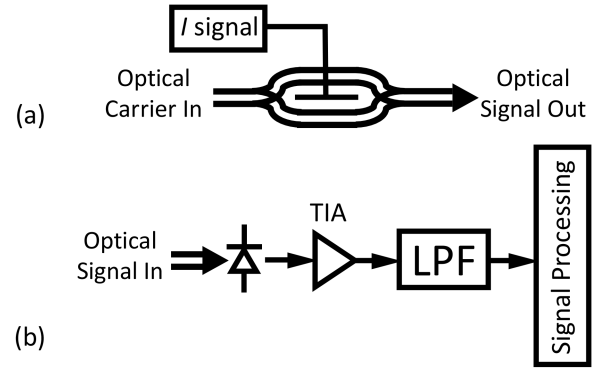


Fig. 5. Direct detection modulator and receiver systems. (a) Mach-Zehnder modulator. (b) Direct detection receiver comprising a positive-intrinsic-negative (PIN) photodetector, transimpedance amplifier (TIA), and lowpass filter (LPF).

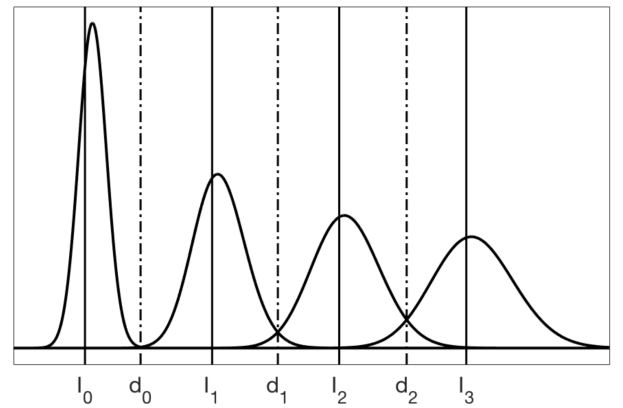


Fig. 6. Representation of simulated probability density functions for a 4-PAM system in the presence of both ASE noise and thermal noise. The noise powers here are artificially enhanced to demonstrate the level-dependence of the noise sources and optimized decision thresholds.

non-Gaussian and signal-dependent. Moreover, in many scenarios discussed here, thermal noise and ASE noise are of comparable strength. This can be seen by analyzing the received current, y_m , for the m th level of an M-PAM constellation,

$$y_m = R|E_m + E_{ASE}|^2 + n_{th} \quad (7)$$

where $E_m = \sqrt{P_m} = \sqrt{2mP_{rx}}$, E_{ASE} is a complex Gaussian random variable with PSD given by Equation (3), and n_{th} is a zero-mean Gaussian random variable with variance, σ_{th}^2 given by Equation (5). For the $m = 0$ case, the output current y_0 is the sum of a central chi-squared random variable and a Gaussian random variable. For $m \neq 0$, y_m corresponds to the sum of a non-central chi-squared random variable and a Gaussian random variable.

Figure 6 demonstrates the level-dependent probability density functions (PDFs) of a directly detected 4-PAM current signal, I_m in the presence of ASE and thermal noise. The distributions are non-Gaussian and the symbol-error probabilities are dependent on the signal power, as shown by the increasingly large tails below the decision thresholds, d_m for large m . In order to calculate the BER of the received signal, one must calculate the PDF

of each y_m , optimize the decision thresholds, and integrate the PDFs to calculate the total BER. The details of this calculation are included in Appendix A.

In this work, we assume that the transmitted M-PAM constellation consists of equally spaced current levels, as in currently implemented 4-PAM systems. The decision thresholds shown in Figure 6 correspond to the overlap of neighboring PDFs and approximate the optimal decision thresholds well for signals with high SNR. More sophisticated methods such as transmit level optimization [35] are not discussed here.

D. Non-Ideal Modulation

In this section we briefly discuss penalties to direct detection and coherent detection systems due to modulator impairments. In this analysis, we assume both systems use dual-drive Mach-Zehnder (DD-MZ) modulators with complementary drive signals to reduce power consumption. We do not discuss some impairments such as finite modulator bandwidth because they can be corrected with small penalties via digital signal processing.

1) *Limited Drive Voltage*: A common limitation of integrated modulators is low modulation efficiency, resulting in a large V_π , which is the voltage required to induce a π phase shift in a single phase shifter. If the complementary drive signals of a DD-MZ modulator are biased at $\pm V_\pi/2$, the modulation transfer function is

$$\frac{E_{out}}{E_{in}} = \sin(\pi V_d/V_\pi) \quad (8)$$

where V_d is the high-frequency drive voltage driven with peak-to-peak voltage of V_π . The arms of the DD-MZ modulator can be driven with a reduced peak-to-peak voltage V_{pp} to decrease power consumption without signal distortion. However, for both direct detection and coherent detection systems this causes an additional insertion loss, $\eta_d = \sin(\pi V_{pp}/2V_\pi)$. While our models of the modulator insertion loss in Section IV take this effect into account, we discuss in further detail the impact of additional transmitter insertion loss in Section V.

2) *Finite Extinction Ratio*: Another important modulator impairment arises from imbalance in the two arms of the DD-MZ modulator. The transfer function of a DD-MZ modulator with power imbalance δ is

$$\begin{aligned} \frac{E_{out}}{E_{in}} &= \left(\frac{1}{2} - \frac{\delta}{2}\right) ie^{-i\pi V_d/V_\pi} - \left(\frac{1}{2} + \frac{\delta}{2}\right) ie^{i\pi V_d/V_\pi} \\ &= \sin(\pi V_d/V_\pi) - i\delta \cos(\pi V_d/V_\pi). \end{aligned} \quad (9)$$

Due to square-law detection in direct detection receivers there is a performance penalty resulting from a finite extinction ratio, $r_{ex} = \delta^2$. While SOI modulators with high extinction ratios have been reported [20], [33], we assume $r_{ex} = -10$ dB, which is realistic for current low-power integrated modulators [36], [37]. Furthermore the impact of a finite extinction ratio on modulator performance depends on the dominant noise statistics at the receiver. These effects are included in the discussion of direct detection receiver statistics in Appendix A.

In coherent systems, power imbalance in the arms of the DD-MZ modulators results in coupling between the in-phase and

quadrature signals. This coupling is deterministic, as shown by Equation (9), and thus the crosstalk can be mitigated by predistorting the modulator drive signals [38]. However, in order to compensate for this crosstalk, the drive voltage of the modulators must be reduced, resulting in an additional insertion loss for M-QAM modulation formats

$$\eta_{ex} = \left(1 - \delta \sqrt{1 - \frac{1}{(\sqrt{M} - 1)^2}}\right)^2 \quad (10)$$

where we have assumed that V_d has peak-to-peak voltage of V_π and both the in-phase and quadrature modulators have equal-magnitude power imbalances δ .

3) *Electronic Crosstalk*: Finally, if DD-MZ modulators are placed closely enough on the transmitter PIC, high-frequency electrical drive signals can couple to each other, resulting in crosstalk between signal streams. However, with careful design, electrical crosstalk can be avoided. For example, if depletion-type silicon DD-MZ modulators are spaced at least 600 μm apart, the crosstalk can be reduced to -30 dB [39]. For modulation schemes utilizing 4-level modulation such as 4-PAM or DP-16-QAM, the resulting input/output bandwidth density is greater than 175 Gb/s/mm at this spacing.

As will be discussed in Section V, the considered coherent and direct detection systems can operate at lower signal-to-noise ratios due to the use of error correcting codes. Crosstalk of -30 dB for the system parameters in Section V results in a penalty of less than 0.3 dB for even the least-tolerant system designs. For this reason we do not include these effects in our calculations.

V. RESULTS AND DISCUSSION

A. Figures of Merit

Traditionally, data center links use direct detection without optical amplification. Since these links are dominated by thermal noise, the receiver sensitivity metric, defined as the minimum optical power necessary to achieve a target BER, is valuable because it allows the optical loss budget to be determined easily. However, future data center architectures that rely on densely packed WDM signals or use optical switches or other lossy components may need to employ optical amplifiers, most likely EDFAs. In some of these cases, amplifier noise may dominate the thermal noise in the receiver. In these cases, the OSNR may be a useful alternate to the optical loss budget as a metric for quantifying overall link performance.

The optical loss budget corresponds directly to the amount of tolerable optical loss in the signal path before the BER exceeds the target BER. The OSNR budget, similarly, corresponds to the total tolerable decrease in OSNR in the signal path before the target BER is exceeded.

B. System Parameter Values

Table II lists the relevant simulation parameters for the simulations that follow. The symbol rate is 56 Gbaud with a total signal bandwidth of 75 GHz in order to reduce the complexity

TABLE II
SYSTEM PARAMETER VALUES

Transmitter	Symbol Rate	56 Gbaud
	Channel Width	75 GHz
	MWS Output Power	25 dBm
	Transmitter Insertion Loss (α_{tx})	-20 dB
	Modulator Extinction Ratio (r_{ex})	-10 dB
	Center Wavelength	1550 nm
Signal Path	Available Bandwidth (C Band)	5 THz
	Signal Path Loss (α_{sp})	-3.5 dB
	Eye Safety Limit (Class 1)	10.1 dBm [40]
	Amplifier Noise Figure	5 dB
	Maximum Amplifier Gain	30 dB
Receiver	AWG Center Frequency Shift	± 0 -150 GHz
	Receiver Insertion Loss (α_{rx})	-7 dB
	Local Oscillator Insertion Loss (α_{LO})	-7 dB
	PIN Photodiode Sensitivity	1 A/W
	TIA Input-referred Noise	30 pA/ $\sqrt{\text{Hz}}$

of pulse shaping in the transmitter. The effective electrical bandwidth of the receiver, Δf_e , is assumed equal to the symbol rate. A 12% overhead associated with coding (7%) and Ethernet (5%) protocols reduces the effective baud rate to 50 Gbaud. A forward error correction (FEC) code, such as RS(255, 239), which has an overhead of 7% and 5.6 dB coding gain with target BER of 1.8×10^{-4} , is assumed here.

In the following simulations, we analyze four different modulation formats: NRZ-OOK, 4-PAM, QPSK, and 16-QAM. The direct detection formats (NRZ-OOK and 4-PAM) are commonly used in data center links today, while the coherent formats (QPSK and 16-QAM) are common in metropolitan area links but have not been extensively used inside data centers.

C. Optical Loss Budget

Figure 7 shows the signal path loss budget for various demultiplexer offsets and amplifier configurations. The subfigures in Figure 7 correspond to demultiplexer center frequency offsets of (a) ± 0 GHz, (b) ± 50 GHz, (c) ± 100 GHz, and (d) ± 150 GHz.

The three compared scenarios are: (1) no amplifier, where optical amplifiers are not used in the link (triangles); (2) booster only, where a booster amplifier immediately follows the transmitter to increase the optical power to the eye-safety limit (squares); and (3) booster and preamplifier, where a booster amplifier immediately follows the transmitter and a preamplifier is placed before the receiver to boost the signal power up to the eye-safety limit (circles).

The dashed lines in Figure 7 correspond to the optical bandwidth-limited per-fiber bit rates for each modulation format. This is calculated by spacing the modulated carriers in the WDM signal as far apart as possible within the entire usable optical bandwidth of 5 THz. For direct detection, the maximum capacity per fiber occurs when the wavelengths are spaced at the

minimum AWG passband width required to ensure that neighboring channels do not drift into the passbands of different receivers for the maximum specified (de)multiplexer shift. This is evident in Figure 7 due to the leftward shift of the dashed lines for direct detection from Figure 7 a to Figure 7 d. Increasing the maximum demultiplexer center frequency offset, corresponding to higher temperature fluctuations, increases the minimum AWG passband width, necessitating a wider wavelength spacing in the WDM signal.

For coherent detection, however, the maximum bit rate per fiber is not determined by the minimum AWG passband width, because interference from nearby wavelengths can be tolerated due to the temperature-insensitive design, as discussed in Section III-B. However, shifts in the (de)multiplexer center frequency do result in decreased loss budget because the power combiner and splitter ratios must be increased. These effects are evident by large jumps in the loss budget for coherent modulation formats at high bit rates per fiber in the presence of large demultiplexer center frequency offsets.

Some highly amplified system implementations have loss budgets that decrease nonlinearly when the bit rate per fiber is increased. For example, in Figure 7 a, both 4-PAM and DP-16-QAM implementations decrease significantly near 25.6 Tb/s per fiber and 3 Tb/s per fiber, respectively. This effect is caused by the dominance of thermal noise in the receiver. In these cases, the ASE noise and thermal noise have similar strengths, where the resultant BER is near, but below, the target BER. Increasing the bit rate per fiber increases the number of wavelengths, which decreases the received power. Since the receiver noise includes a significant contribution from thermal noise, the ASE noise must be decreased significantly to compensate, decreasing the loss budget significantly. The absolute limit on the bit rate per fiber for these systems can be calculated by analyzing the receiver sensitivity solely in the presence of thermal noise, taking into account the total power at the receiver and number of wavelengths.

From Figure 7 it is clear that unamplified direct detection links will be difficult to scale beyond 400 Gb/s per fiber with co-packaged optical interfaces due to high loss and poor receiver sensitivity. While both unamplified direct and coherent detection systems with lower transmitter PIC losses may have larger loss budgets than shown in Figure 7, the per-fiber bit rate of direct detection systems is limited by the maximum eye-safe optical power in the signal path. Indeed, even for systems that utilize a booster amplifier immediately following the transmitter PIC, the loss budget for 800 Gb/s-per-fiber systems is less than 4 dB.

Coherent systems not only provide a high loss budget, but can also support more wavelengths, due to the temperature-insensitive design. For example, in the presence of ± 150 GHz demultiplexer center frequency offsets, amplified systems based on DP-16-QAM can support 12.8 Tb/s per fiber with a loss budget of ~ 9 dB while links based on 4-PAM can support less than 1.3 Tb/s per fiber. Even at the low bit rate of 400 Gb/s per fiber, systems using QPSK offer over 20 dB higher loss budget than NRZ-OOK systems.

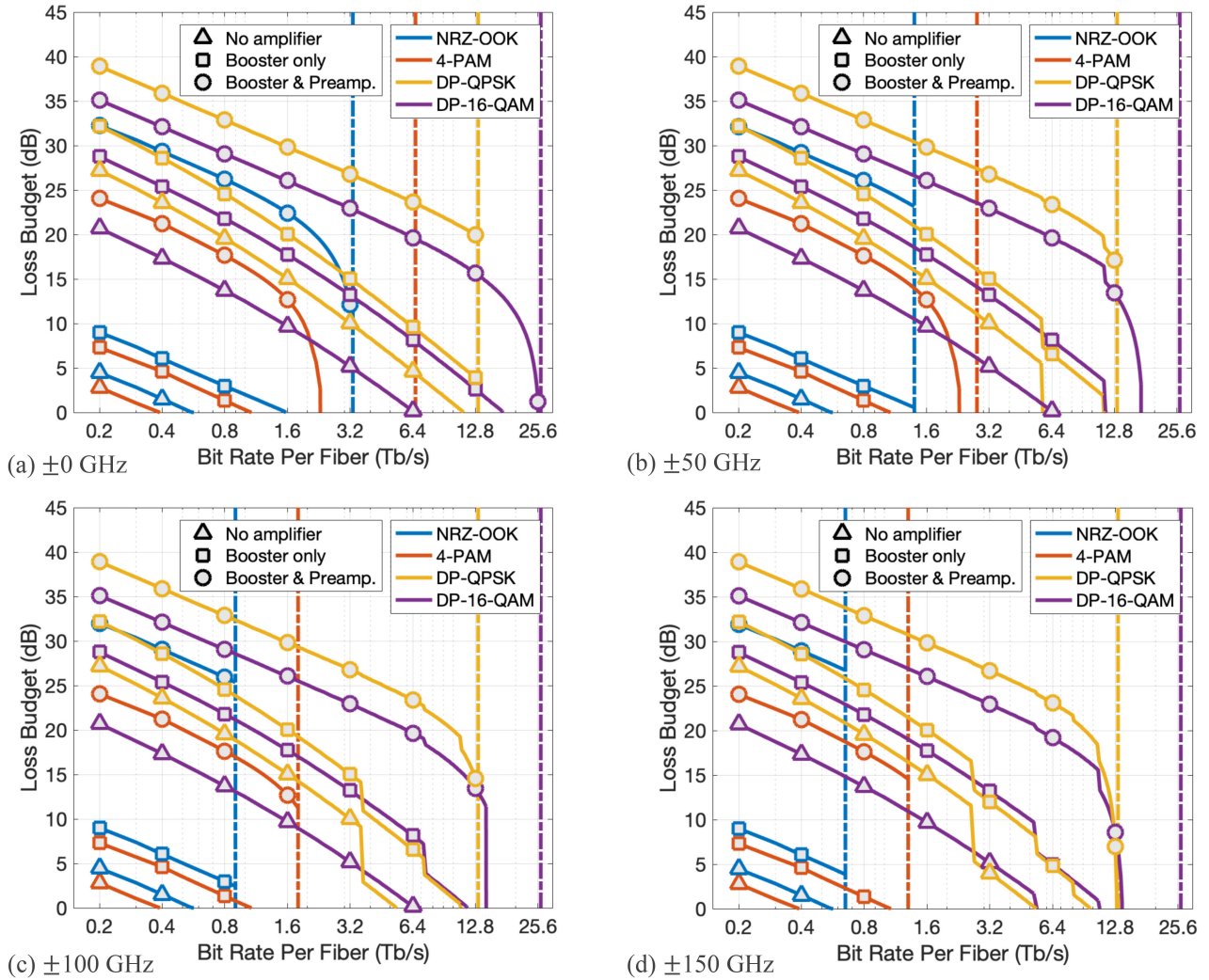


Fig. 7. Signal path loss budget for various demultiplexer center frequency shifts. Demultiplexer center frequency shifts of (a) ± 0 GHz, (b) ± 50 GHz, (c) ± 100 GHz, and (d) ± 150 GHz are compared for system designs implemented with no amplifiers (triangles), a booster amplifier only (squares), and both a booster and preamplifier (circles). Modulation formats include non-return-to-zero on-off keying (NRZ-OOK), 4-ary pulse amplitude modulation (4-PAM), quadrature phase shift keying (QPSK), and 16 quadrature amplitude modulation (16-QAM).

D. OSNR Budget

Figure 8 shows the signal path OSNR budgets for various demultiplexer offsets and amplifier configurations. The subfigures in Figure 8 correspond to demultiplexer center frequency offsets of (a) ± 0 GHz, (b) ± 50 GHz, (c) ± 100 GHz, and (d) ± 150 GHz. The OSNR budget is a useful metric for future systems that utilize optical amplifiers to compensate for substantial optical losses, such as in optical switches. We consider the second scenario from the previous section, corresponding to a system that only has a booster amplifier and assume that the WDM signal power at the receiver is equal to the eye-safety limit.

The OSNR budget presented in Figure 8 is similar to the loss budget at low bit rates per fiber for systems that employ both a booster amplifier and preamplifier, as shown in Figure 7. At these bit rates, additional power combiners and splitters in the transmitter and receiver PICs are unnecessary because the

(de)multiplexer passbands are wide enough to accommodate large temperature fluctuations. Thus, the signal path optical loss, which is fully compensated by the preamplifier, is equivalent to a degradation in the OSNR.

By contrast, for coherent systems at high bit rates per fiber, the OSNR budget differs significantly from the loss budget. This effect is demonstrated in Figure 8 d for bit rates per fiber greater than ~ 3 Tb/s. Here, due to the design of the thermally insensitive demultiplexing scheme, losses in both the transmitter and receiver PICs increase as the bit rate per fiber increases. The additional receiver loss does not impact the OSNR budget because the noise in the receiver is dominated by ASE, which is also attenuated. However, additional losses in the transmitter PIC reduce the OSNR at the output of the booster amplifier. Therefore, the OSNR budgets in Figure 8 are lower than the amplified loss budgets in Figure 7 when additional losses are introduced into the transmitter.

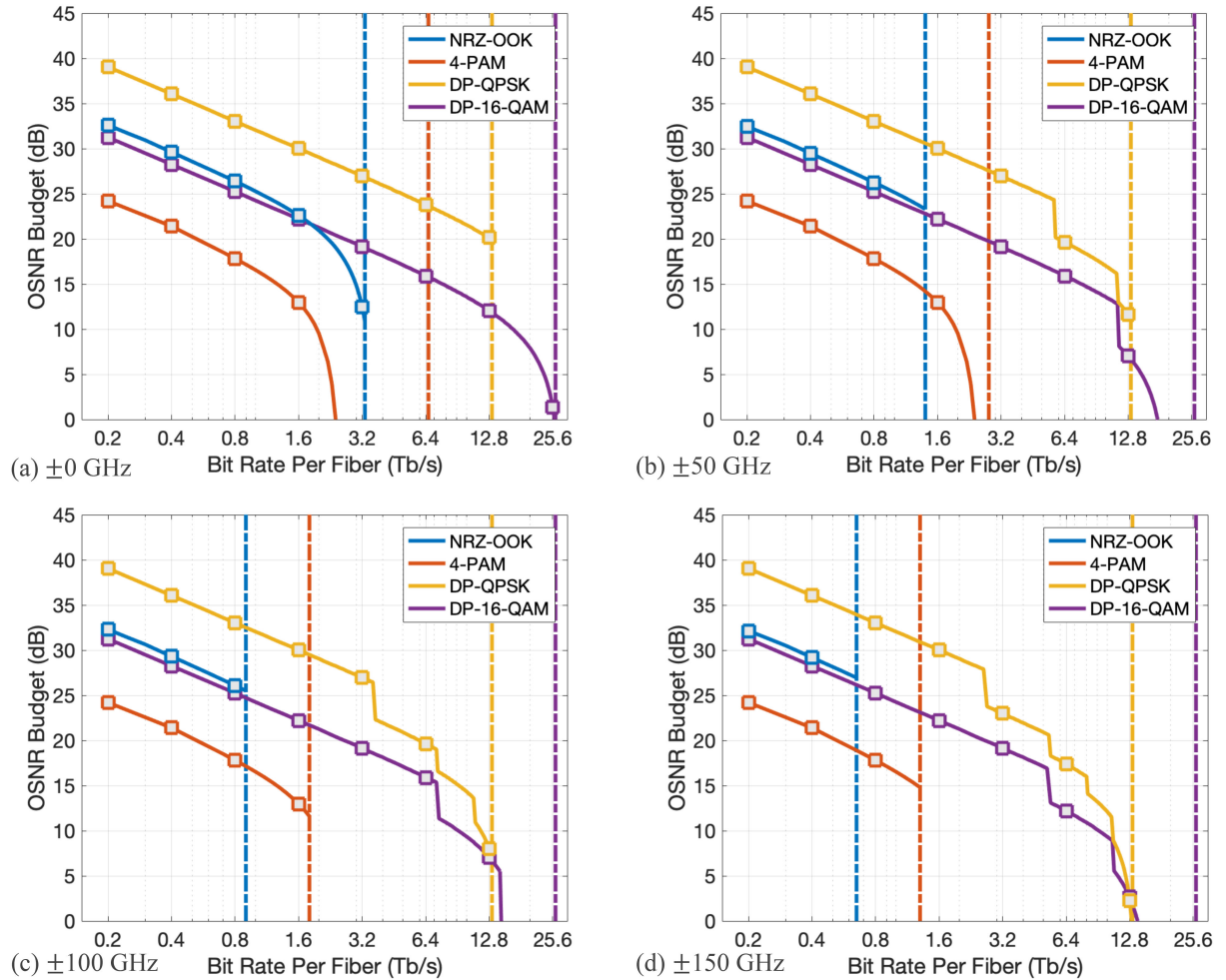


Fig. 8. Signal path OSNR budget for various demultiplexer center frequency shifts. Demultiplexer center frequency shifts of (a) ± 0 GHz, (b) ± 50 GHz, (c) ± 100 GHz, and (d) ± 150 GHz are compared for a system that utilizes a booster amplifier immediately after the transmitter PIC to increase the WDM signal power to the eye-safety limit (squares). Modulation formats include non-return-to-zero on-off keying (NRZ-OOK), 4-ary pulse amplitude modulation (4-PAM), quadrature phase shift keying (QPSK), and 16 quadrature amplitude modulation (16-QAM).

Interestingly, from Figure 8, amplified direct detection systems can provide large OSNR budgets. However, as with the loss budget, for large demultiplexer center frequency offsets, the limited optical bandwidth significantly reduces the achievable bit rate per fiber. For example, for ± 150 GHz demultiplexer center frequency shifts, DP-16-QAM can scale to over 13 Tb/s while 4-PAM systems are limited to less than 1.3 Tb/s.

VI. CONCLUSION

We have proposed a scalable intra-data center link architecture based on co-packaged switch interfaces that can tolerate (de)multiplexer shifts induced by temperature fluctuations. We analyze direct detection and coherent detection links to determine the loss budget and OSNR budget for unamplified and amplified systems. Unamplified intra-data center links based on direct detection are not a scalable solution due to their poor receiver sensitivity and limited ability to scale to higher WDM channel counts. Even introducing amplifiers into direct detection links may only allow bit rates per fiber to scale by a factor

of two or three. Coherent detection can provide over 20 dB loss budget for unamplified systems. Amplified coherent detection can scale to bit rates per fiber exceeding 12.8 Tb/s, an order of magnitude larger than amplified direct detection systems.

APPENDIX A

M-PAM RECEIVER WITH NON-GAUSSIAN STATISTICS

As discussed in the main text, the addition of ASE noise in direct detection systems results in an electrical signal with non-Gaussian statistics at the receiver. Here we analyze and discuss the signal PDF in the presence of both ASE noise and thermal noise. We assume there is negligible inter-symbol interference, infinite extinction ratio, and ideal sampling. Equation (7) can be normalized to the total ASE power in the signal bandwidth such that the normalized received signal is

$$Y_m = \frac{y_m}{I_{ASE}} = |\sqrt{\lambda_m} + \tilde{E}_{ASE}|^2 + N_{th} = L_m + N_{th}. \quad (11)$$

where $I_{ASE} = RS_{sp}\Delta f_e$ is the RMS noise current from ASE noise in the receiver bandwidth, Δf_e , the ASE PSD, S_{sp} , is

defined in Equation (3) and the level-dependent non-centrality parameter is

$$\lambda_m = \frac{I_m}{I_{ASE}} + r_{ex} \left(\frac{M-1-m}{M-1} \right) \frac{I_M}{I_{ASE}} \quad (12)$$

where the effect of a finite modulator extinction ratio, r_{ex} , is included. We have also introduced the complex normal variable, $\tilde{E}_{ASE} \sim N(0,1)$ and the real normal variable $N_{th} \sim N(0, \sigma_{th}/I_{ASE})$, where σ_{th} is defined in Equation (5).

From this formulation it is clear that the first term, L_m is a non-central chi-squared random variable with non-centrality parameter λ_m . However, the number of degrees of freedom, k , of L_m depends on the total optical bandwidth of the ASE noise, Δf_o , incident onto the PIN photodetector. The conservative approximation $k \approx 2\Delta f_o/\Delta f_e$, where k , is an integer, can be made if the optical bandwidth is much larger than the electrical bandwidth. This condition is satisfied for nearly all the systems considered in Figure 7. In the few situations where the electrical bandwidth is comparable to the optical bandwidth, such as in Figure 7 a for the booster amplified and pre-amplified direct detection cases, the thermal noise dominates the ASE-ASE beat noise in the receiver, so the effect of any inaccuracy in the approximation is negligible.

We can check that this model is consistent with common Gaussian approximations of the level-dependent PDFs for systems dominated by ASE noise. The variance of the received current, $\sigma_{y_m}^2$, assuming the thermal noise n_{th} and extinction ratio r_{ex} are negligible, is given by

$$\begin{aligned} \sigma_{y_m}^2 &= I_{ASE}^2 \text{Var}(L_m) \\ &= R^2 S_{sp}^2 \Delta f_e^2 (2k + 4\lambda_m) \\ &= 4R^2 S_{sp}^2 \Delta f_e \Delta f_o + 4R^2 P_m S_{sp} \Delta f_e. \end{aligned} \quad (13)$$

Here, the variance of the received current is composed of exactly the same two terms as the Gaussian approximation [41], where the first term corresponds to ASE-ASE beat noise and the second term corresponds to signal-ASE beat noise.

Then, the PDFs of the two random variables in Equation (11), L_m and N_{th} , are

$$f_{L_m}(y) = \frac{1}{2} e^{-(y+\lambda_m)/2} \left(\frac{y}{\lambda_m} \right)^{k/4-1/2} I_{k/2-1}(\sqrt{\lambda_m y}) \quad (14)$$

$$f_{N_{th}}(y) = \frac{1}{\sqrt{2\pi\sigma_N^2}} e^{-\frac{y^2}{2\sigma_N^2}} \quad (15)$$

where $I_\nu(y)$ is a modified Bessel function of the first kind and the normalized variance of N_{th} is $\sigma_N^2 = \sigma_{th}^2/I_{ASE}^2$.

Finally, since L_m and N_{th} are independent noise sources, the PDF of the normalized received signal, Y_m , can be determined by a convolution of the PDFs in Equations 14 and 15 such as

$$f_{Y_m}(y) = f_{L_m}(y) * f_{N_{th}}(y). \quad (16)$$

In order to optimize the $M-1$ decision thresholds, we sample the PDF in Equation (16) and calculate the values of y for which the PDFs of the M PDFs overlap. The intersection of the PDFs approximates the optimal decision threshold in the case of

Gaussian-like PDFs. Figure 6 demonstrates the optimal decision levels for an ASE-dominated direct detection receiver.

To calculate the symbol-error probability, P_e , we integrate the tails of each of the M PDFs up to the decision thresholds. We assume that the receiver operates in the large SNR regime so that the errors are dominated by nearest neighbors. For a Gray-coded M-PAM constellation the bit-error ratio can be calculated with $BER \approx P_e/\log_2(M)$.

REFERENCES

- [1] "Cisco global cloud index: Forecast and methodology, 2016–2021," White Paper, Feb. 2018.
- [2] M. Rakowski, "Silicon photonics platform for 50G optical interconnects," in *Proc. Cadence Photon. Summit Workshop*, 2017, pp. 3–4.
- [3] C. Schmidt, C. Kottke, R. Freund, F. Gerfers, and V. Jungnickel, "Digital-to-analog converters for high-speed optical communications using frequency interleaving: Impairments and characteristics," *Opt. Express*, vol. 26, no. 6, pp. 6758–6770, Mar. 2018.
- [4] C. Kachris, K. Bergman, and I. Tomkos, *Optical Interconnects for Future Data Center Networks*. Berlin, Germany: Springer, 2012.
- [5] A. Bechtolsheim, "Scaling the cloud network," presented at the Open Compute Project 2018 U.S. Summit, San Jose, CA, USA, Mar. 20–21, 2018.
- [6] "400 Gb/s landscape potential interfaces and architectures," Nexans White Paper, Jun. 2018.
- [7] A. Ghiasi, "Large data centers interconnect bottlenecks," *Opt. Express*, vol. 23, no. 3, pp. 2085–2090, Feb. 2015.
- [8] A. Ghiasi, *400GBase-LR8: A Proposal for 10 km Objective Using 50 Gb/s PAM4 Signaling, IEEE 802.3bs Task Force*, May 2015.
- [9] K. Sato, "Realization and application of large-scale fast optical circuit switch for data center networking," *J. Lightw. Technol.*, vol. 36, no. 7, pp. 1411–1419, Apr. 2018.
- [10] K. Yamada, *Silicon Photonic Wire Waveguides: Fundamentals and Applications*. Berlin, Germany: Springer, 2011, pp. 1–29.
- [11] L. Pavesi and D. J. Lockwood, "Silicon photonics III," in *Topics in Applied Physics*, vol. 122. Berlin, Germany: Springer, 2016.
- [12] A. Abdollahinia *et al.*, "Temperature stability of static and dynamic properties of 1.55 μm quantum dot lasers," *Opt. Express*, vol. 26, no. 5, pp. 6056–6066, Mar. 2018.
- [13] J. Bovington, S. Srinivasan, and J. E. Bowers, "Athermal laser design," *Opt. Express*, vol. 22, no. 16, pp. 19 357–19 364, Aug. 2014.
- [14] K. Okamoto, "Wavelength-division-multiplexing devices in thin SOI: Advances and prospects," *IEEE J. Sel. Topics Quantum Electron.*, vol. 20, no. 4, pp. 248–257, Jul. 2014.
- [15] T. Tekin, N. Pleros, R. Pitwon, and A. Hakansson, *Optical Interconnects for Data Centers*. Cambridge, U.K.: Woodhead, 2016.
- [16] X. Wang *et al.*, "Athermal silicon arrayed waveguide grating with polymer-filled slot structure," in *Proc. 5th IEEE Int. Conf. Group IV Photon.*, Sep. 2008, pp. 253–255.
- [17] L. Carroll, D. Gerace, I. Cristiani, and L. C. Andreani, "Optimizing polarization-diversity couplers for Si-photonics: Reaching the -1dB coupling efficiency threshold," *Opt. Express*, vol. 22, no. 12, pp. 14 769–14 781, Jun. 2014.
- [18] R. Marchetti *et al.*, "High-efficiency grating-couplers: Demonstration of a new design strategy," *Sci. Rep.*, vol. 7, no. 1, 2017, Art. no. 16670.
- [19] Z. Lu *et al.*, "Broadband silicon photonic directional coupler using asymmetric-waveguide based phase control," *Opt. Express*, vol. 23, no. 3, pp. 3795–3808, Feb. 2015.
- [20] G. F. R. Chen, J. R. Ong, T. Y. L. Ang, S. T. Lim, C. E. Png, and D. T. H. Tan, "Broadband silicon-on-insulator directional couplers using a combination of straight and curved waveguide sections," *Sci. Rep.*, vol. 7, no. 1, 2017, Art. no. 7246.
- [21] K. K. Lee, D. R. Lim, L. C. Kimerling, J. Shin, and F. Cerrina, "Fabrication of ultralow-loss Si/SiO₂ waveguides by roughness reduction," *Opt. Lett.*, vol. 26, no. 23, pp. 1888–1890, Dec. 2001.
- [22] P. Dumon *et al.*, "Linear and nonlinear nanophotonic devices based on silicon-on-insulator wire waveguides," *Jpn. J. Appl. Phys.*, vol. 45, no. 8S, 2006, Art. no. 6589.

- [23] S. Pathak, M. Vanslebrouck, P. Dumon, D. V. Thourhout, and W. Bogaerts, "Compact SOI-based polarization diversity wavelength demultiplexer circuit using two symmetric AWGs," in *Proc. 38th Eur. Conf. Exhib. Opt. Commun.*, Sep. 2012, pp. 1–3.
- [24] H. Li *et al.*, "Preliminary investigation of an SOI-based arrayed waveguide grating demodulation integration microsystem," *Sci. Rep.*, vol. 4, May 2014, Art. no. 4848.
- [25] C. Xiong, D. M. Gill, J. E. Proesel, J. S. Orcutt, W. Haensch, and W. M. J. Green, "Monolithic 56 Gb/s silicon photonic pulse-amplitude modulation transmitter," *Optica*, vol. 3, no. 10, pp. 1060–1065, Oct. 2016.
- [26] X. Xiao *et al.*, "High-speed, low-loss silicon Mach–Zehnder modulators with doping optimization," *Opt. Express*, vol. 21, no. 4, pp. 4116–4125, Feb. 2013.
- [27] H. Subbaraman *et al.*, "Recent advances in silicon-based passive and active optical interconnects," *Opt. Express*, vol. 23, no. 3, pp. 2487–2511, Feb. 2015.
- [28] G. Li *et al.*, "Ultralow-loss, high-density SOI optical waveguide routing for macrochip interconnects," *Opt. Express*, vol. 20, no. 11, pp. 12 035–12 039, May 2012.
- [29] H. Guan *et al.*, "Compact and low loss 90° optical hybrid on a silicon-on-insulator platform," *Opt. Express*, vol. 25, no. 23, pp. 28 957–28 968, Nov. 2017.
- [30] P. Dong *et al.*, "224-Gb/s PDM-16-QAM modulator and receiver based on silicon photonic integrated circuits," in *Proc. Opt. Fiber Commun. Conf. Expo. Nat. Fiber Opt. Eng. Conf.*, Mar. 2013, pp. 1–3.
- [31] J. Lin, H. Sepehrian, L. A. Rusch, and W. Shi, "CMOS-compatible silicon photonic IQ modulator for 84 Gbaud 16QAM and 70 Gbaud 32QAM," in *Proc. Opt. Fiber Commun. Conf.*, 2018, Paper. Tu2E.4.
- [32] B. Milivojevic *et al.*, "112 Gb/s DP-QPSK transmission over 2427 km SSMF using small-size silicon photonic IQ modulator and low-power CMOS driver," in *Proc. Opt. Fiber Commun. Conf. Expo. Nat. Fiber Opt. Eng. Conf.*, Mar. 2013, pp. 1–3.
- [33] H. Zhu *et al.*, "Optimized silicon QPSK modulator with 64-Gb/s modulation speed," *IEEE Photon. J.*, vol. 7, no. 3, pp. 1–6, Jun. 2015.
- [34] C. Doerr *et al.*, "Single-chip silicon photonics 100-Gb/s coherent transceiver," in *Proc. Opt. Fiber Commun. Conf.*, Mar. 2014, pp. 1–3.
- [35] J. K. Perin, M. Sharif, and J. M. Kahn, "Sensitivity improvement in 100 Gb/s-per-wavelength links using semiconductor optical amplifiers or avalanche photodiodes," *J. Lightw. Technol.*, vol. 34, no. 23, pp. 5542–5553, Dec. 2016.
- [36] L. Yang and J. Ding, "High-speed silicon Mach-Zehnder optical modulator with large optical bandwidth," *J. Lightw. Technol.*, vol. 32, no. 5, pp. 966–970, Mar. 2014.
- [37] M. Webster *et al.*, "An efficient MOS-capacitor based silicon modulator and CMOS drivers for optical transmitters," in *Proc. 11th Int. Conf. Group IV Photon.*, Aug. 2014, pp. 1–2.
- [38] A. Napoli, M. M. Mezghanni, S. Calabr, R. Palmer, G. Saathoff, and B. Spinnler, "Digital predistortion techniques for finite extinction ratio IQ Mach-Zehnder modulators," *J. Lightw. Technol.*, vol. 35, no. 19, pp. 4289–4296, Oct. 2017.
- [39] L. Jiang, X. Chen, K. Kim, G. de Valicourt, Z. R. Huang, and P. Dong, "Electro-optic crosstalk in parallel silicon photonic Mach-Zehnder modulators," *J. Lightw. Technol.*, vol. 36, no. 9, pp. 1713–1720, May 2018.
- [40] *Safety of Optical Fibre Communication Systems, IEC 60825-2: Safety Laser Products*, vol. 3.2, Dec. 2010.
- [41] P. M. Becker, A. A. Olsson, and J. R. Simpson, *Erbium-Doped Fiber Amplifiers: Fundamentals and Technology*. Amsterdam, The Netherlands: Elsevier, 1999.

Brandon Buscaino (S'17) received the B.S. degree in physics and the M.S. degree in electrical engineering both from Stanford University, Stanford, CA, USA, in 2015 and 2016, respectively, where he is currently working toward the Ph.D. degree. His current research interests include coherent optical fiber communications, intra-data center link design, and co-packaged optical interfaces.

Brian D. Taylor received the B.S. degree in physics from the University of Rochester, Rochester, NY, USA, in 1996 and the M.S. degree in electrical engineering from Northwestern University, Evanston, IL, USA, in 2000. He is currently an Optical Transceiver Engineer with Inphi Corporation, Westlake Village, CA, USA.

Joseph M. Kahn (F'00) received the A.B., M.A., and Ph.D. degrees in physics from the University of California, Berkeley (UC Berkeley), Berkeley, CA, USA, in 1981, 1983, and 1986, respectively. From 1987 to 1990, he was with AT&T Bell Laboratories, Crawford Hill Laboratory, Holmdel, NJ, USA. He demonstrated multi-Gb/s coherent optical fiber transmission systems, setting world records for receiver sensitivity. From 1990 to 2003, he was a faculty with the Department of Electrical Engineering and Computer Sciences, UC Berkeley, performing research on optical and wireless communications. Since 2003, he has been a Professor of electrical engineering with Stanford University, where he heads the Optical Communications Group. His current research interests include fiber-based imaging, spatial multiplexing, rate-adaptive and spectrally efficient modulation and coding methods, coherent detection and associated digital signal processing algorithms, digital compensation of fiber nonlinearity, and free-space systems. He was the recipient of the National Science Foundation Presidential Young Investigator Award in 1991. From 1993 to 2000, he was a Technical Editor for the IEEE PERSONAL COMMUNICATIONS MAGAZINE. From 2009 to 2014, he was an Associate Editor for the IEEE/OSA JOURNAL OF OPTICAL COMMUNICATIONS AND NETWORKING. In 2000, he helped found StrataLight Communications, where he was a Chief Scientist from 2000 to 2003. StrataLight was acquired by Opnext, Inc., in 2009.